

Influence of Polymer Aggregation and Liquid Immiscibility on Morphology Tuning by Varying Composition in PffBT4T-2DT/Non-Fullerene Organic Solar Cells

Zeinab Hamid, Andrew Wadsworth, Elham Rezasoltani, Sarah Holliday, Mohammed Azzouzi, Marios Neophytou, Anne A. Y. Guilbert, Yifan Dong, Mark S. Little, Subhrangsu Mukherjee, Andrew A. Herzing, Helen Bristow, R. Joseph Kline, Dean M. DeLongchamp, Artem A. Bakulin, James Durrant, Jenny Nelson and Iain McCulloch*

Z. Hamid, Dr. A. Wadsworth, Dr. S. Holliday, Y. Dong, Dr. M. S. Little, H. Bristow, Dr. A. A. Bakulin, Prof. J. Durrant, Prof. I. McCulloch
Department of Chemistry and Centre for Plastic Electronics, Imperial College London, London, W12 0BZ, United Kingdom
Email: zeinab.hamid13@imperial.ac.uk

Dr. E. Rezasoltani, M. Azzouzi, Dr. A. A. Y. Guilbert, Prof. J. Nelson
Department of Physics and Centre for Plastic Electronics, Imperial College London, London, SW7 2AZ, United Kingdom

Dr. M. Neophytou, Prof. I. McCulloch
Physical Sciences and Engineering Division, KAUST Solar Center (KSC), King Abdullah University of Science and Technology (KAUST), KSC Thuwal 23955-6900, Saudi Arabia.

Dr. S. Mukherjee, Dr. A. A. Herzing, Dr. R. J. Kline, Dr. D. M. DeLongchamp
Material Measurement Laboratory, National Institute of Standards and Technology, Gaithersburg, Maryland 20899, USA

Keywords: organic photovoltaics, morphology, calorimetry, phase behavior, nonfullerene

The temperature dependent aggregation behavior of PffBT4T polymers used in organic solar cells plays a critical role in the formation of a favorable morphology in fullerene-based devices. However, there has been little investigation into the impact of donor/acceptor ratio on morphology tuning, especially for non-fullerene acceptors (NFAs). Herein, the influence of composition on morphology is reported for blends of PffBT4T-2DT with two NFAs, O-IDTBR and O-IDFBR. The monotectic phase behavior inferred from differential scanning calorimetry provides qualitative insight into the interplay between solid-liquid and liquid-liquid demixing. Transient absorption spectroscopy suggests that geminate recombination dominates charge decay and that the decay rate is insensitive to composition, corroborated by negligible changes in open-circuit voltage. Exciton lifetimes are also insensitive to composition, which is attributed to the signal being dominated by acceptor excitons which are formed and decay in domains of similar size and purity irrespective of composition. A

hierarchical morphology is observed, where the composition dependence of size scales and scattering intensity from resonant soft X-ray scattering (R-SoXS) is dominated by variations in volume fractions of polymer/polymer rich domains. Results suggest an optimal morphology where polymer crystallite size and connectivity are balanced, ensuring a high probability of hole extraction via such domains.

1. Introduction

Single-junction organic photovoltaic (OPV) devices have made significant improvements in efficiency, with certified power conversion efficiencies (PCEs) rapidly improving from 13 % to over 15 % over the past two years,^[1-5] thus exceeding the 15 % threshold considered to be required for commercial viability.^[6] Extensive research has led to the availability of a myriad of organic semiconductors for OPV applications. These are combined into blends comprising an electron donor and an electron acceptor, which typically are a polymer and a small molecule, respectively, although other combinations can be used. Small molecule acceptors are subdivided into two classes, namely fullerene and non-fullerene acceptors (NFAs). While the former dominate due to properties such as isotropic electron transport, disadvantages such as costly synthesis, poor optical absorption in the visible region of the solar spectrum and morphological instability led to the development of NFAs.^[7] The most widely investigated blend is that based on PCBM as a fullerene acceptor, combined with P3HT, a wide band-gap polymer.^[8] In addition to the efforts aimed at optimizing acceptor properties by designing NFAs, low band-gap polymers based on alternating donor and acceptor moieties were designed to reduce the donor band gap in order to improve light-harvesting in the abundant region of the visible spectrum.

While P3HT:PCBM in particular, and many polymer:fullerene blends in general, are now well understood in terms of how materials' structures affect device performance and stability, this was achieved following a time-consuming device optimization and characterisation approach. Now that a wider variety of materials are available, and much higher efficiencies

possible, increasing effort is being devoted to developing a rational approach to materials design, selection and device optimization.^[9–14] One of the key parameters to maximising efficiency is the morphology of the light-absorbing active layer. Differences in compatibility between binary blend materials lead to the possibility of active layers having at least three phases when the donor is crystalline: pure crystalline donor domains, pure acceptor aggregates (either amorphous or crystalline), as well as an amorphous mixed phase.^[12,15] While pure domains are important for ensuring efficient charge percolation to the electrodes, mixed phases are favorable as they improve exciton dissociation, but excessive mixing is undesirable as it also increases the probability of recombination.^[16] Both thermodynamic and kinetic factors are at play and govern microstructure formation. Thermodynamic factors include solubility limits, the energetic barrier to crystallization and the strength of the repulsive amorphous-amorphous interactions, which govern the binodal, or liquid-liquid (L-L) miscibility gap.^[17] Kinetic factors include drying rates and the kinetics of crystal nucleation and growth.^[18,19]

Knowledge of the miscibility of each OPV blend component within the other is important for rational material selection and device optimization. The binodal provides quantitative information regarding the degree of phase separation (if any) and domain composition in the amorphous mixed phase, although the presence of crystals must be corrected for.^[13] A low miscibility system (large L-L two-phase region) will lead to large, pure domains of each component, and thus the morphology will need to be kinetically frozen in a mixed state to enhance charge generation. The stability of such a microstructure is then determined by how far this composition is from the binodal at the relevant temperature,^[13] as well as by the glass transition temperature (T_g) and by the factors controlling molecular diffusion.^[20]

Similarly to amorphous domains, rational understanding of optimal crystalline microstructure is equally important; a balance needs to be struck between crystallite purity, size and interconnectivity to improve transport and reduce recombination.^[16,21–23] A model for

rational understanding of optimal donor/acceptor (D/A) ratios in crystalline/crystalline polymer/small molecule blends was proposed based on eutectic temperature-composition ($T-\phi$) diagrams determined from differential scanning calorimetry (DSC), whereby compositions that are more acceptor-rich relative to the eutectic composition (i.e., hyper-eutectic with respect to acceptor content), are found to maximise the short-circuit current (J_{SC}) by affording improved electron percolation.^[24] Such phase behavior has since been observed for a wide range of blends incorporating P3HT, with either fullerene or non-fullerene blends,^[8,25] and has also been observed for blends incorporating other wide band gap polymers such as pBTTT and F8TBT.^[16,26,27]

Similar investigations are needed for blends incorporating higher-performing low band gap polymers such as PffBT4T-2OD, also known as PCE11. Binary blends combining PffBT4T-2OD with fullerene acceptors display several advantages, such as the possibility of processing from hydrocarbon solvents, and a robust microstructure leading to high efficiencies even in thick films.^[21,28] However, studies on the phase behavior of such blends and its impact on optimal D/A ratios in devices are lacking. $T-\phi$ data have been reported for PffBT4T-2OD blended with PCBM as acceptor, but there was no comment on the resultant eutectic.^[29] It is thought that the temperature-dependent aggregation behavior of PffBT4T polymers is a key factor behind the favorable morphology in as-cast devices, leading to the formation of highly pure polymer crystallites around 40 nm in size for a variety of processing parameters (spin speed, temperature and concentration) and fullerenes.^[21,30] Blends of PffBT4T polymers (namely PffBT4T-2OD or its longer side-chain derivative, PffBT4T-2DT) with rhodanine-flanked non-fullerene acceptors show comparable crystalline polymer domains,^[31,32] but offer several advantages over their fullerene counterparts, namely higher voltages, reduced voltage losses,^[31] improved stability towards thermal and burn-in degradation,^[33] and also show enhancement in efficiency and shelf life when processed from hydrocarbon solvents.^[34] D/A

ratio tuning and its impact on morphology in blends of the PffBT4T polymers with either fullerenes or NFAs is however not explored in detail.^[31,32]

To this purpose, here we focus on elucidating the effects of D/A ratio tuning on the morphology of devices incorporating PffBT4T-2DT with O-IDTBR. In contrast to the observation of eutectic $T-\phi$ phase behavior in crystalline/crystalline blends so far, DSC thermograms of neat materials and blends suggest monotectic phase behavior (indicating low liquid miscibility), with a monotectic point at intermediate composition. Such behavior has been referred to schematically before in the context of OPVs.^[13] Using a combination of microscopy, spectroscopy and X-ray techniques, we investigate the changes in morphology and correlate them to the $T-\phi$ diagram. We also briefly explore the effect of acceptor crystallinity by using the less crystalline acceptor O-IDFBR which has a twisted backbone due to the bulkier phenyl moieties of the indenofluorene unit compared to thiophene flanking aryl groups in indacenodithiophene. The observed phase behavior allowed a qualitative rationalization of the optimal morphology in terms of the varying interplay between solid-liquid (S-L) and liquid-liquid (L-L) phase separation as a function of composition. Results suggest that around the monotectic composition in blends with O-IDTBR, it is likely that polymer aggregation (S-L demixing) during casting is more dominant compared to L-L demixing such that it limits the extent of phase separation. In contrast, at more acceptor-rich compositions, a more phase separated morphology occurs, likely due to L-L demixing playing a more significant role during solution drying. S-L demixing may occur simultaneously and the lower solution viscosity (due to lower polymer concentration) would extend polymer crystal growth time, which would contribute to the increased coarseness. While the $T-\phi$ diagram of blends incorporating the less crystalline acceptor O-IDFBR is also monotectic, there are some differences in the dependence of acceptor bulk crystallinity on composition. However, the dependence of device performance on composition is similar for both acceptors, suggesting that acceptor crystallinity plays a less significant role in governing the morphology compared to polymer crystallization (S-L

demixing) and the strength of donor/acceptor interactions (which govern L-L demixing). It is important to note that an accurate picture of the dynamics during casting, namely whether or not S-L and L-L demixing occur simultaneously, or if either mechanism completely dominates, requires in-situ investigation of film formation, which is beyond the scope of this work. The interest herein is constructing a qualitative model based on DSC results, a simple and accessible characterisation technique, to understand the dependence of device performance on the morphology as a function of D/A ratio in monotectic blends. Quantitative results from grazing incidence wide angle scattering (GIWAXS) and R-SoXS support the suggested trend in the degree of phase separation as a $\approx 50\%$ increase in size scale, 150% increase in scattering intensity, and 67% higher polymer crystallinity occur at a hyper-monotectic composition (with respect to acceptor content). R-SoXS and TEM additionally suggest a complex hierarchical morphology. The observed reduction in J_{SC} and PCE is attributed to the combination of a larger degree of phase separation and low polymer concentration, which reduces the probability of efficient hole extraction as the crystalline polymer domains become isolated.

2. Results

2.1. Bulk Phase Behavior: Deviation from Common Eutectic Blends

DSC is used to examine the T - ϕ diagram of PffBT4T-2DT combined with O-IDTBR as NFA (see **figure 1a** for chemical structures). DSC thermograms of the neat materials and the blends, as well as the resultant T - ϕ diagram, are shown in **Figure 1b** and **figure 1c** (the same data from second heating cycles is shown in **Figure S1**). Pure PffBT4T-2DT shows one sharp melt with an onset temperature T_m at $260\text{ }^\circ\text{C}$ and an enthalpy of fusion ΔH_f of 22 J g^{-1} . Pure O-IDTBR shows one sharp melt at $227\text{ }^\circ\text{C}$ ($\Delta H_f = 46\text{ J g}^{-1}$) preceded by a cold crystallization ($\Delta H_{cc} = 21\text{ J g}^{-1}$) at $T_{cc} = 111\text{ }^\circ\text{C}$. No eutectic is observed in the resultant T - ϕ diagram, in contrast to reports of crystalline/crystalline binaries thus far.^[8,16,24–27,35] In a eutectic blend, the melting temperature of either one or both components is progressively depressed as the

amount of the other component increases in the blend, up to a eutectic composition, at which the two liquidus curves meet.

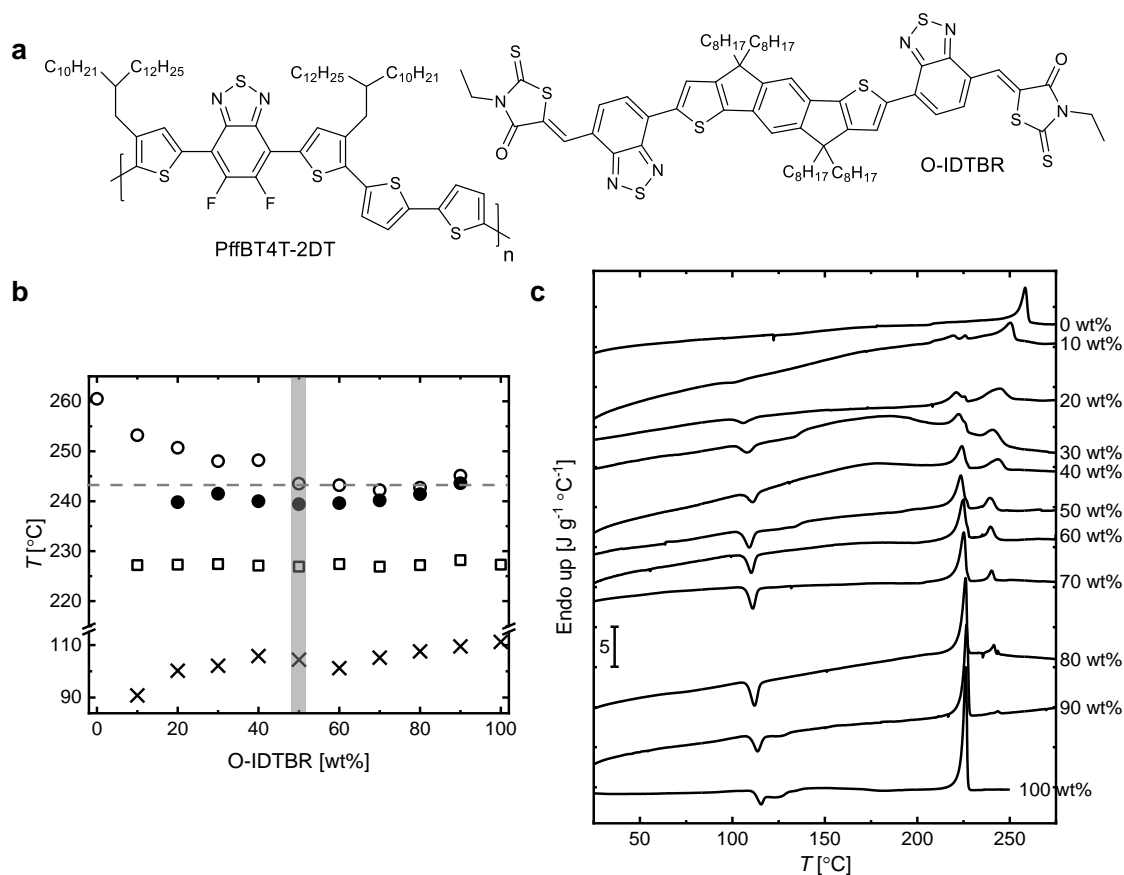


Figure 1. (a) Chemical structures of PffBT4T-2DT and O-IDTBR; (b) T - ϕ diagram of PffBT4T-2DT:O-IDTBR constructed from DSC first heating thermograms; empty circles correspond to the polymer melt endset temperature; filled circles correspond to the peak of the low-temperature shoulder of the polymer endotherm from (10 to 40) wt % O-IDTBR, and to the peak temperature of the polymer endotherm from (60 to 90) wt % O-IDTBR; empty squares indicate the endset melting temperature of O-IDTBR and crosses denote the onset temperature of acceptor cold-crystallization; vertical and horizontal lines are guides to the eye and roughly denote monotectic composition and temperature, respectively; (c) DSC first heating thermograms of PffBT4T-2DT:O-IDTBR; thermograms are offset for clarity and the concentration of O-IDTBR is indicated on the right.

Upon cooling below the eutectic temperature in a typical eutectic blend, both components crystallize simultaneously from the eutectic liquid. Fast solidification rates, such as the rate of drying during solution casting, limit crystal growth leading to a finely phase separated

crystalline microstructure. Herein it is observed that, while O-IDTBR displays no melting point depression, the polymer melt is depressed up to ≈ 50 wt % (used hereafter to refer specifically to mass %) O-IDTBR, at which point the depression stops. This suggests that the mixed liquid phase in equilibrium with the polymer crystals becomes saturated in O-IDTBR. In contrast to a eutectic, the liquidus curves which trace the melting point progression of each component do not meet. The shape of the $T-\phi$ diagram reported here indicates monotectic phase behavior. A schematic of such phase behavior is depicted in **Figure S2**. A monotectic blend displays strong liquid-liquid immiscibility, such that the miscibility gap ‘penetrates’ the liquidus curve of the higher-melting component.^[36,37]

Upon cooling a blend exhibiting monotectic phase behavior, three characteristic reactions occur upon cooling from the homogeneous melt. The first occurs once the temperature decreases below the critical temperature and corresponds to liquid-liquid phase separation into donor-rich and acceptor-rich liquid phases ($L \rightarrow L_D + L_A$, where D and A denote donor and acceptor, respectively). The second is the monotectic reaction, where the liquid at monotectic composition ϕ_{mo} transforms into solid S_D and liquid L_A ($L_D \rightarrow S_D + L_A$). Lastly, the eutectic reaction occurs: $L_A \rightarrow S_D + S_A$. The phases present at RT after cooling from the melt are relatively pure polymer and acceptor crystalline phases, as well as an amorphous polymer-rich phase (the amount of which will depend on the cooling kinetics).

The solidification dynamics which lead to these phases differ depending on the starting D/A ratio. At donor-rich compositions below ϕ_{mo} , polymer crystallization (S-L demixing) most likely initiates microstructure formation. In the case of a large barrier to nucleation, the onset of crystallization may be supercooled such that L-L demixing would occur first,^[36] but this is unlikely for the system of interest here given the polymer’s strong tendency to aggregate. Such S-L demixing will push the composition of the remaining liquid phase into the L-L two-phase region. Thus initial D/A ratios which fall within the miscibility gap (above ϕ_{mo}) are

expected to show the strongest degree of coarsening as L-L demixing possibly dominates microstructure formation. In contrast, for compositions $\phi \leq \phi_{mo}$, crystallization likely plays a more important role, which would freeze-in a smaller length scale.

Evidently, morphology formation during device fabrication occurs under different conditions as active layers are formed from solution, not from the melt. It should be noted, however, that the solvent does not dramatically affect the size and location of the L-L two-phase region, which is governed by donor/acceptor interactions.^[18] As such, in combination with the established understanding of the aggregation behavior of PffBT4T polymers, it is reasonable to use the phase behavior obtained from DSC to provide an idea of the interplay between L-L and S-L demixing during solution casting.

Using the morphology picture from the phase behavior, it is thus expected that spun cast active layers will display a coarser morphology when the composition is hyper-monotectic with respect to acceptor content (i.e., > 50 wt % acceptor). To evaluate the effect of the suggested changes in morphology, we now focus on device performance as a function of composition.

2.2. Device Performance as a Function of D/A Ratio

Table 1. *J-V* characteristics and thicknesses of PffBT4T-2DT:O-IDTBR devices; active layer solution concentration is 15 mg mL⁻¹ unless stated otherwise.

PffBT4T-2DT <i>M_w</i> [kDa]	O-IDTBR [wt %]	<i>J_{sc}</i> [mA cm ⁻²]	<i>V_{oc}</i> [V]	<i>FF</i>	average PCE ^{a)} [%]	Thickness ^{b)} [nm]
41 kDa	41	10.1	1.03	0.49	5.1 (±0.48)	104
	50	11.2	1.04	0.52	6.1 (±0.77)	85
	55	10.9	1.03	0.52	5.9 (±0.57)	88
	64	9.3	1.02	0.57	5.4 (±0.29)	77
	74	6.0	1.00	0.54	3.3 (±0.30)	72
55 kDa	41 ^{o)}	11.8	1.01	0.62	7.3 (±0.18)	60
	50	13.4	1.03	0.57	7.9 (±0.51)	69
	64	10.3	1.03	0.59	6.2 (±0.60)	66
	74	8.7	1.02	0.60	5.3 (±0.48)	68

a) The average PCE and uncertainties (standard deviation) were calculated over 7 to 12 devices; b) Thickness values are averaged over at least three measurements for each device, taking into account the centre and edge of the active layer; c) 13 mg mL⁻¹ active layer solution concentration was used to reduce the thickness from 77 nm to 60 nm

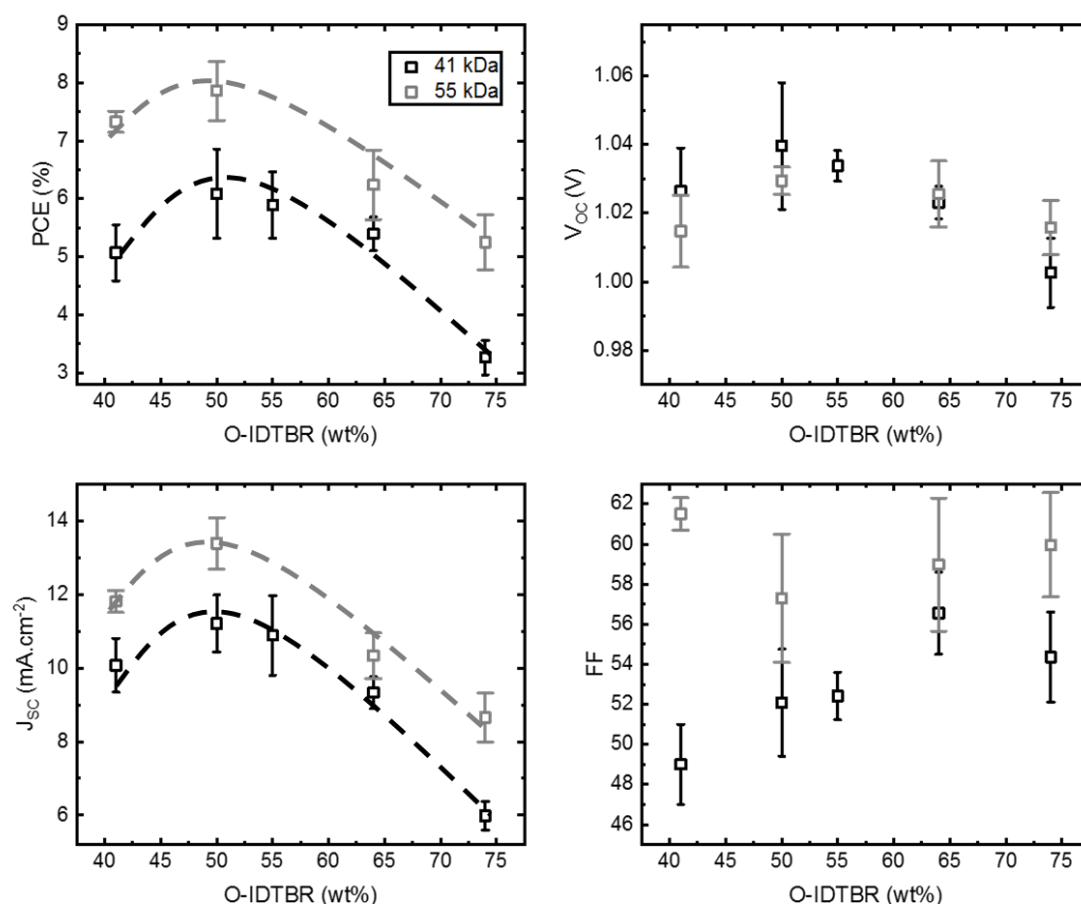


Figure 2. Device parameters of PffBT4T-2DT:O-IDTBR as a function of D/A ratio and polymer molecular weight (41 kDa and 55 kDa); dashed lines were manually constructed as guides to the eye; average values and standard deviations were calculated over 7 to 14 devices.

Current-voltage (J - V) characteristics of devices as a function of D/A ratio for two polymer molecular weights are summarized in **Table 1** and **Figure 2**. The maximum efficiency, obtained with a PffBT4T-2DT mass average relative molecular mass (M_w) of 41 kDa, is lower than that previously reported for the same blend (6.9 % vs. 10 %).^[31] Although maximizing the efficiency for a single blend was not central to this study, a higher M_w batch of the

polymer was prepared (55 kDa), achieving maximum efficiencies more comparable to literature (8.4 %) and showing similar trends to the 41 kDa batch in the dependence of device parameters on composition (the partial T - ϕ diagram was also determined and shown in **Figure S3**). Power conversion efficiency (PCE) is found to be largely dictated by J_{SC} . It can be seen that PCE and J_{SC} both peak around (50 to 55) wt % O-IDTBR (devices fabricated using the lower M_w batch show comparable performance at 50 wt % & 55 wt % acceptor). From the J - V characteristics (Table 1), it can be seen that devices fabricated with the 41 kDa polymer batch with a 50 wt % acceptor loading display, on average, an efficiency of 6.1 ± 0.8 % with a J_{SC} of 11.2 mA m^{-2} and fill factor (FF) of 0.52. At higher and lower acceptor concentrations, average J_{SC} and PCE drop with a minimum observed at 74 wt % O-IDTBR (6.0 mA cm^{-2} and 3.3 %, respectively). FF varies very little, going from 0.49 ± 0.02 at 41 wt % to 0.54 ± 0.02 at 74 wt % O-IDTBR.

With the 55 kDa batch, similar behavior occurs in that average J_{SC} and PCE both peak at 50 wt % acceptor (13.4 mA cm^{-2} and 7.9 %). Average FF reaches its maximum of 0.62 at 41 wt % O-IDTBR, and remains around 0.59 ± 0.02 upon further acceptor addition.

Comparing device performances of the two M_w , the lower J_{SC} and FF with the 41 kDa polymer can be attributed to sub-optimal morphology with the lower M_w batch of PffBT4T-2DT. This has been observed for PffBT4T-OD:PC₇₁BM, where lower M_w was found to induce larger, lower purity domains with poorer π - π stacking (as measured from the lower coherence length from GIWAXS), leading to reduced FF and J_{SC} .^[30]

To understand the origin behind the dependence of J_{SC} on D/A ratio, it is important to first consider the effect of thickness variations, induced by different solution compositions. It is worth noting that it is difficult to efficiently control active layer thickness for such blend types incorporating polymers with strong temperature dependent aggregation (TDA) properties, where a variation in thickness, of up to 20 nm, was observed within a single film.

Thickness values as a function of composition and M_w are reported in Table 1. Blends with the low M_w batch vary in thickness by ≈ 30 nm, while the higher M_w batch displays smaller thickness fluctuations (only up to ≈ 10 nm, given the use of a lower solution concentration for the blend richest in polymer). Considering that the same J_{SC} -composition dependence is observed for both M_w , despite a difference in the magnitude of thickness variation, suggests that the trend in J_{SC} is dominated by the effect of composition, rather than thickness.

No significant change in FF is observed. Similarly, open-circuit voltage (V_{OC}) varies little as a function of composition. V_{OC} is generally considered to be independent of the morphology in the bulk. However, it has been observed to vary as a result of morphological changes which affect the D/A interface (e.g. in terms of interfacial area or aggregation).^[38,39] Since a difference in interfacial area is expected as the composition is varied, External Quantum Efficiency (EQE) and Electroluminescence (EL) spectroscopy were used to probe whether or not there are differences in voltage loss contributions as the ratio changes. Results show little variation as a function of composition, supporting the idea that the influence of morphology changes on J_{SC} is the main factor behind the dependence of performance on D/A ratio (see SI **Figure S4** and **Table S1** for a more detailed discussion of EQE and EL results). While the phase behavior from DSC suggests a coarser morphology above the monotectic composition in slow-dried thick films, we now turn towards an in-depth characterization of thin-films prepared under similar conditions as devices.

2.3. Thin-Film Micro- and Nano-structure

To investigate thin-film morphological changes as a function of composition, we performed grazing incidence wide angle X-ray scattering (GIWAXS), resonant soft X-ray scattering (R-SoXS) and low-angle annular dark field STEM (LAADF-STEM) of thin films of 41 kDa PffBT4T-2DT:O-IDTBR.

The packing characteristics of the polymer donor and the molecular acceptor were measured by GIWAXS. The 2D GIWAXS scattering patterns and sector averaged 1D profiles are

shown in **Figure S5**. The GIWAXS data indicate that for all the samples the polymer crystallites exhibit a strong preferential edge-on orientation with respect to the substrate with up to 4 orders of the (h00) diffraction peaks due to the lamella separation parallel to the surface normal. In contrast, a more face-on orientation is observed for the O-IDTBR with a strong in-plane (100) peak around 0.4 \AA^{-1} . Volume-normalized pole figures from the (100) diffraction peaks of PffBT4T-2Dt and O-IDTBR are shown in **Figure S6**. The relative degree of crystallinity (rDoC) assessed from these pole figures is shown in **Figure 3a**.

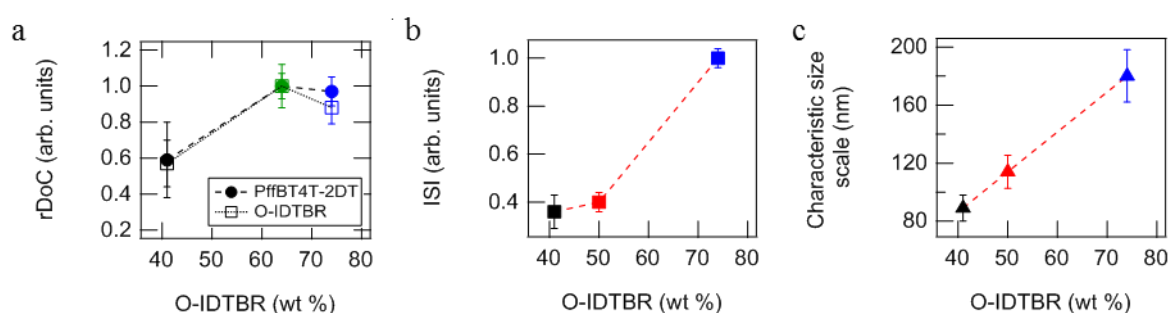


Figure 3. (a) Relative degree of crystallinity (rDoC) of PffBT4T-2DT and O-IDTBR from GIWAXS for 41 kDa PffBT4T-2DT:O-IDTBR at 41 wt %, 64 wt % and 74 wt %; (b) relative average purity and (c) size scales extracted from R-SoXS for 41 kDa PffBT4T-2DT:O-IDTBR at 41 wt %, 50 wt % and 74 wt %. Uncertainties in rDoC are from standard deviation in film thickness and sample length measurements. Uncertainties in size scales and scattering intensities are from standard deviation of the respective values from R-SoXS data acquired at high material contrast energies.

Importantly, an increase of the rDoC of the polymer as well as the acceptor is observed for D/A ratios above ϕ_{mo} . This result suggests that polymer and acceptor aggregation plays a dominant role in governing the composition dependence of morphology and consequently the compositional dependence of J_{SC} as well. As speculated above, L-L demixing is likely to play a more important role in the initial stages of drying at higher acceptor loading compared to S-L demixing. However, the higher degree of crystallinity at 74 wt % acceptor can be explained by the occurrence of polymer crystallization at a later stage during drying from the phase-separated polymer-rich liquid phase.

R-SoXS was used to quantify the length scale of phase separation as well as relative scattering intensities. Scattering profiles obtained at 284 eV are shown in **Figure S7** and the extracted size scales are shown in **Figure 3b**. A good fit was obtained using two log-normal peaks. The low-q peak, indicating micrometer size scales, likely originates from surface roughness and has a negligible contribution to the integrated scattering intensity (ISI). In agreement with the more uniform thickness at the highest acceptor loading, this peak disappears at 74 wt % O-IDTBR. The high-q peak originates from D/A phase separation. Extracted characteristic length scale values for 41 wt %, 50 wt % and 74 wt % O-IDTBR are \approx (90, 115 and 180) nm respectively, which is similar to previous reports of blends incorporating PffBT4T donors with fullerenes.^[21,30,40] Such size scales are quite large but the broad peaks imply a broad dispersion which likely arises from a hierarchical morphology. The **normalized** relative integrated scattering intensity (ISI) is shown in **Figure 3c**. These ISI values are a measure of the contrast between two phases and the respective volume fractions.^[41] A step-like increase in ISI is observed for D/A ratios above ϕ_{mo} .

To summarise, the breadth of the R-SoXS peaks suggests the occurrence of a hierarchical morphology at all three compositions probed, with a gradual increase in median size scale. The occurrence of a multi-length scale morphology and different volume fractions makes it difficult to quantify the degree of phase separation at different acceptor loading. However, the fact that the largest median size scale at 74 wt % O-IDTBR also exhibits the highest ISI relative to the other compositions indicates a more phase separated morphology.

LAADF-STEM was used to further consolidate the morphology picture (**Figure 4**). In agreement with R-SoXS, results suggest the occurrence of a hierarchical morphology given the observation of features \approx 100 nm to 200 nm in size. However, we do not observe a significant difference in the size of these features as a function of composition, as expected based on the varying degree of phase separation. In fact, obtaining a complete morphological picture from electron microscopy for such a blend system is complicated by the low level of

contrast given the similarity in chemical composition of both components. Analysis is also complicated by the fact that the images are a 2D projection of a 3D morphology.

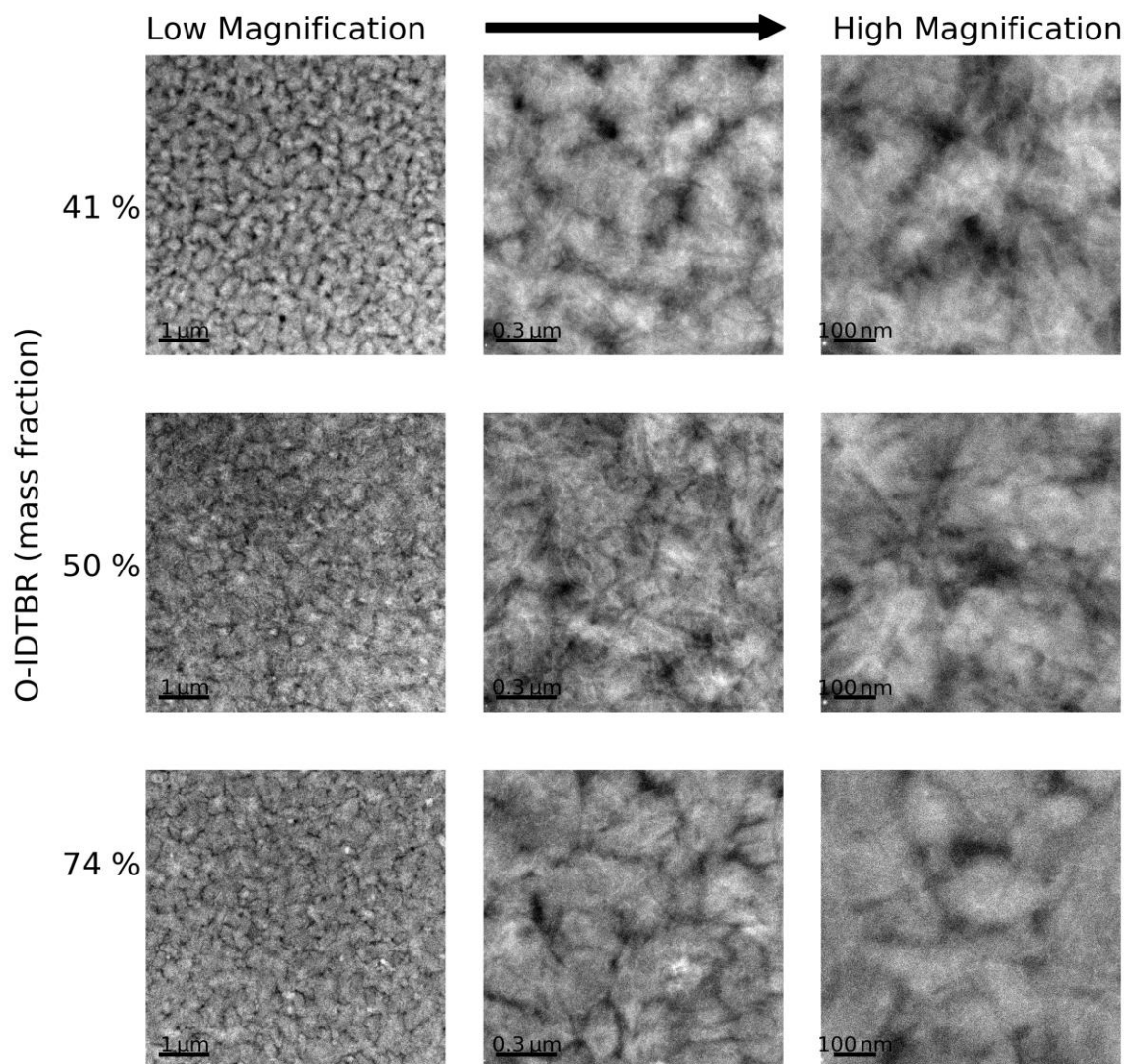


Figure 4. LAADF-STEM images of PffBT4T-2DT:O-IDTBR blends using the 41 kDa batch, where the images intensity scales with density.

The results from real-space microscopy and scattering studies thus agree reasonably well. Our morphology characterisation results reveal a complex hierarchical morphology and are consistent with the degree of phase separation expected from our phase diagram. For active layer solutions with compositions below the monotectic ϕ_{mo} , the suggested dominance of S-L

demixing means there is less time for crystal/aggregate growth, which would freeze-in a smaller length scale, lower crystallinity and lower composition variation and/or pure phases with different volume fractions. The occurrence of L-L demixing to a stronger extent in the 74 wt % blend ($\phi > \phi_{mo}$) (i.e. deeper quench depth) is consistent with the coarser morphology, higher degree of aggregation/crystallinity, and higher degree of phase separation. Hence, the large drop in J_{SC} upon increasing acceptor content from (50 to 74) wt % could suggest that device performance becomes limited by the exciton diffusion length as excitons need to travel further to reach a D/A interface, which would lead to a longer exciton lifetime at 74 wt %. However, this doesn't seem to be the case, as will be discussed in the next section. In order to elaborate further the morphology image and its impact on the trend in J_{SC} , we investigate the dynamics of charge generation and recombination.

2.4. Charge Generation and Recombination

Photoluminescence spectroscopy (PL) was employed to elucidate the impact of the observed changes in morphology on exciton dissociation, while femtosecond-transient absorption spectroscopy (fs-TAS) was used to elucidate their impact on charge generation and recombination in blends with the 41 kDa batch.

Extracting values for PL quenching efficiency (PLQE) is complicated by overlapping absorption profiles (**Figure S8**) which prevents selective excitation of either donor or acceptor. Thus an 'overall' PLQE is extracted by **normalizing** the PL intensity with respect to the emission from neat O-IDTBR (PL spectra were initially **normalized** to the absorption at the excitation wavelength). It should be noted that neat O-IDTBR was cast from hot solution to match the conditions used for the neat polymer and polymer/acceptor blend films. An overall PLQE of $(80 \pm 5) \%$ occurs between 41 wt % and 64 wt % O-IDTBR (**Figure 5a**; PL spectra are shown in Figure S8). The relatively low quenching efficiency has been previously attributed to the formation of large, highly pure PffBT4T polymer domains.^[33] At 74 wt %

acceptor, PLQE decreases to $\approx 65\%$. The occurrence of a coarser microstructure at higher acceptor loading is indeed expected to lead to a reduction in PLQE as excitons need to travel further before dissociating at a D/A interface, thus the probability of exciton dissociation is reduced. However, the 15% drop in PLQE on going from (41 to 64) wt% O-IDTBR to 74 wt% is not sufficient to explain the 42% decrease in J_{SC} and PCE. Hence, in order to further understand the trend in J_{SC} , TAS was used to investigate the dynamics of charge generation and recombination.

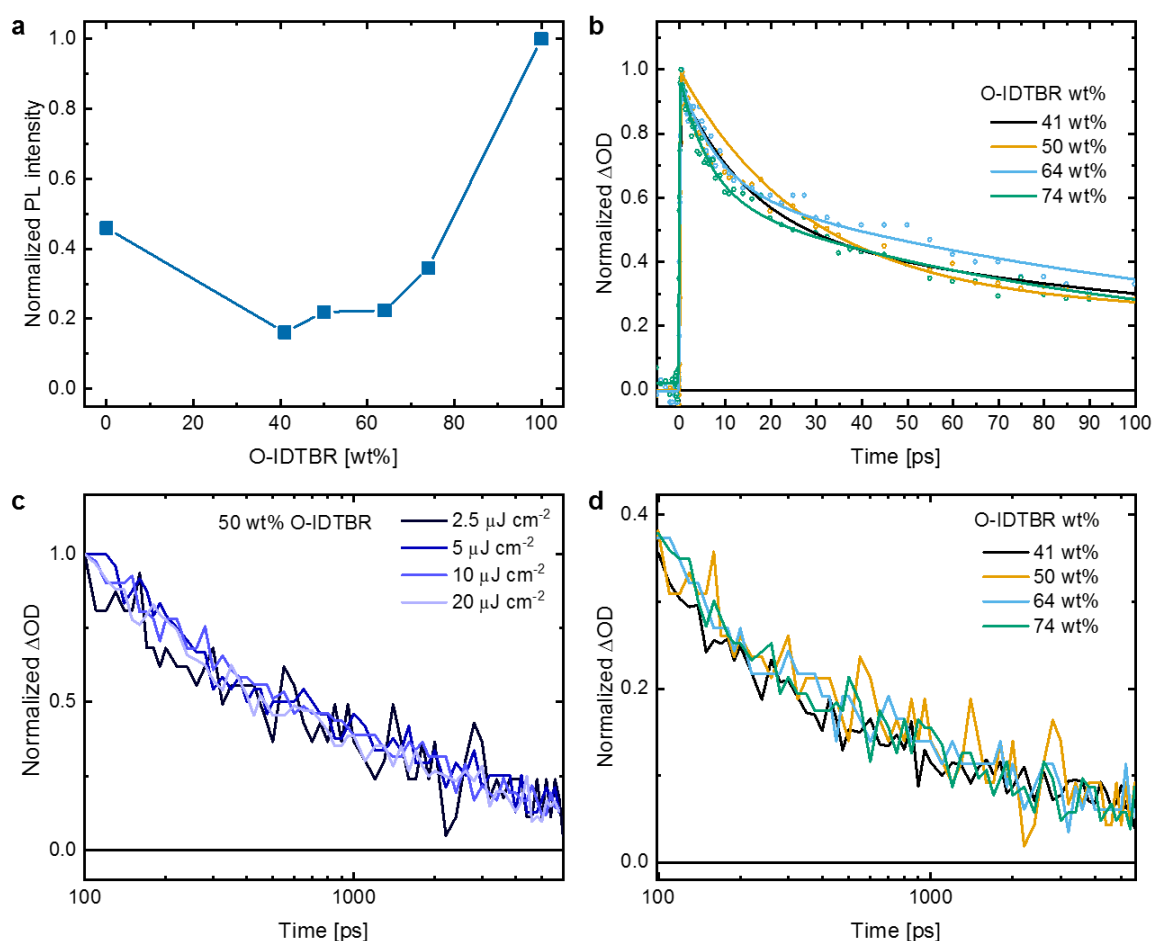


Figure 5. (a) PL intensity as a function of acceptor wt % in blends of PffBT4T-2DT:O-IDTBR excited at 630 nm; (b) Transient absorption kinetics probed at 1125 nm where the kinetics are **normalized** at 0 s. Similar decay rate is observed in all the blends; (c) Transient absorption kinetics probed at 1050 nm for the PffBT4T-2DT:O-IDTBR blend with an acceptor of 50 wt% at various pump fluences ranging from (2.5 to 20) $\mu J cm^{-2}$. The kinetics are normalized at 100 ps where most excitons have decayed to the ground state. (d) Transient

absorption kinetics at 1050 nm for PffBT4T-2DT:O-IDTBR blends with different ratios with the kinetics normalized at 0 ps. All films were fabricated using the 41 kDa polymer batch and excited at 650 nm for TAS measurements.

Transient absorption spectra as a function of time delay of the neat materials and the 41 wt %, 50 wt %, 64 wt % and 74 wt % O-IDTBR blends excited at 650 nm are shown in **Figure S9**.

Polymer and acceptor exciton absorption in the neat films peaks at 1050 and 1125 nm,

respectively. Due to the broad and featureless responses of donor and acceptor

exciton/polaron excited states, we could not use global analysis procedures to accurately

decompose the transient absorption spectra and unambiguously link the dynamics to specific

excited states.^[42] Nonetheless, the shift in maximum transient absorption to shorter

wavelengths over time in the blends can be clearly related to polaron formation. To compare

the dynamics of excitons in different materials, we therefore focus on short-time (sub-100ps)

transients in the 1125 nm region as transient absorption response at this time/wavelength has

mostly excitonic character. To address the dynamics of charges we instead compare long time

(>100 ps) transients in the 1050 nm region.

Figure 5b shows the transient absorption dynamics probed at 1125 nm, where both PffBT4T-

2DT and O-IDTBR singlet excitons absorb while the polaron absorption is less pronounced.

Surprisingly, only negligible changes in exciton lifetime in blends are observed, with an

average lifetime of (22 ± 4) ps. As such, the trend in exciton dynamics cannot be directly

related to the significant morphological changes reflected in both size scale and ISI observed

from R-SoXS. The invariance in lifetime with increased coarseness suggests that the signal is

dominated by excitons which are travelling within domains of similar composition, and also

size (if these domains are practically pure). Assuming a three-phase morphology, we must

consider crystalline donor (D) domains, acceptor aggregates, and the amorphous D-rich

matrix. **Given the difference in molecular size between a polymer and a small molecule, the**

former is more sensitive to processing conditions such as the rate and temperature at which

solidification occurs. While a crystalline small molecule like O-IDTBR may easily crystallize/aggregate within a narrow temperature range and maintain a similar degree of crystallinity under various rates of solidification, the crystallization of a macromolecule occurs over a wider temperature range and is more rate-dependent. These two variables affect both crystal purity and size. The purity of small molecule acceptor aggregates is thus not expected to change much as a function of initial composition, in contrast to polymer domains. This is reflected in the asymmetry of the binodal in polymer/small molecule binaries, such that the small molecule-rich branch of the binodal is nearly vertical, meaning that the composition of the small molecule-rich liquid varies little as a function of temperature (modelled in Figure S2). As a result, the purity of acceptor crystals/aggregates formed from the acceptor-rich liquid L_A is similar irrespective of quench depth. These IDTBR crystals are also expected to be pure,^[43,44] which means that they must also display similar sizes within the (41 to 74) wt % D/A composition range in order to explain the invariance in exciton lifetime. As such, it seems the fast drying kinetics during spin-coating limit the growth of acceptor crystals at higher acceptor loading. While the lifetime of excitons generated in polymer/polymer-rich domains is expected to vary as polymer domain purity changes, the results from TAS suggest that the signal is dominated by excitons generated in acceptor domains. This is reasonable given the much higher absorption coefficient of IDTBR relative to PffBT4T polymers.^[43]

At long times (> 100 ps), the kinetics probed at 1050 nm provide insight on the decay of polarons as all excitons have decayed by that time and exciton absorption is red-shifted from this wavelength. By varying the pump fluence between $2.5 \mu\text{J cm}^{-2}$ and $20 \mu\text{J cm}^{-2}$, the kinetics at 1050 nm are found to be fluence-independent, indicating geminate recombination (**Figure 5c** for the 50 wt % blend; see **Figure S10** for the other compositions). This was also observed for PffBT4T-2OD:EH-IDTBR, where the dominance of geminate recombination was attributed to the modest LUMO/LUMO offset,^[33] such that following exciton

dissociation, there is little energetic driving force to promote electron/hole transport away from the interface.^[45] These loosely bound charges were found to recombine geminately at the same rate irrespective of acceptor concentration (**Figure 5d**), with a half-lifetime ≈ 300 ps.

The invariance in the decay lifetime of charges across the composition series correlates with the largely invariant V_{OC} with respect to composition (Table 1), such that there is little change in the driving force for charge separation at the interface.

To summarize, the trend in PL quenching supplements the morphology picture inferred from GIWAXS and according to which the polymer crystallinity/aggregation increases by 67 % on going from (41 to 50) wt % to 74 wt % O-IDTBR. This is further supplemented by an increase of R-SoXS scattering intensity as well as size scales indicating an increase in domain purity. The negligible change in exciton lifetime, as observed in TAS measurements, is interpreted as being an effect of an invariance in the size of pure acceptor domains across this composition range. In consequence, the trend in relative domain purity when going from (41 to 50) wt % to 74 wt % O-IDTBR must be associated with the changes in polymer aggregation. The lower solution viscosity at 74 wt % O-IDTBR compared to (41 to 50) wt % facilitates molecular diffusion, allowing the formation of purer polymer domains. This translates into a larger difference in contrast between phases, which was observed in R-SoXS as higher scattering intensity. While higher purity is beneficial for charge extraction, the concomitant drop in J_{SC} is attributed to isolated crystalline polymer domains at low polymer loading, leading to a lower probability of efficient hole extraction. These changes in morphology as a function of composition are illustrated schematically in **figure 6**.

Finally, to understand the role of acceptor crystallinity on controlling the morphology via composition tuning, we investigated the phase behavior and device performance of 41 kDa PffBT4T-2DT with the amorphous acceptor O-IDFBR.

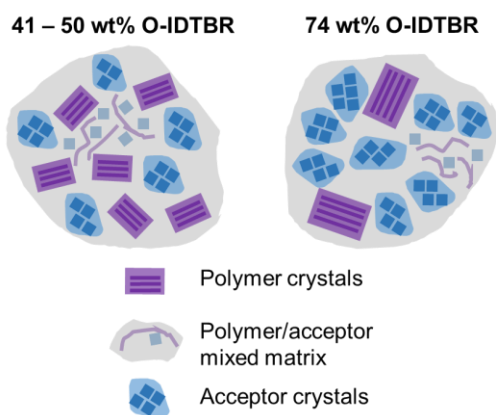


Figure 6. Schematic cartoon illustrating the change in morphology as acceptor concentration is increased above the monotectic composition around 50 wt%.

2.5. Effect of Acceptor Crystallinity

O-IDFBR is known to have a weaker tendency to aggregate compared to O-IDTBR,^[46] similarly to FBR, which has been reported to achieve reduced non-radiative voltage losses when blended with PffBT4T-2DT.^[31] Blends with O-IDFBR also display monotectic behavior (**Figure S11**), but the acceptor shows a negligible degree of crystallinity compared to O-IDTBR. The difference in acceptor phase behavior is illustrated in **Figure S12**: in contrast to the complete crystallization of O-IDTBR at all compositions probed, O-IDFBR crystallization is inhibited from 60 wt% to 90 wt % O-IDFBR and is almost completely suppressed from 10 wt% to 60 wt %. The monotectic composition occurs at a more acceptor-rich loading compared to blends with O-IDTBR (around 60 wt % O-IDFBR). This is likely due to the lower melting temperature of O-IDFBR and weaker polymer/acceptor repulsive interactions with O-IDFBR compared to O-IDTBR,^[35] such that the polymer-rich melt tolerates a higher NFA content. Devices utilizing the low M_w polymer with O-IDFBR were also fabricated for 50 wt %, 64 wt % and 74 wt % acceptor (**Figure S13** and **Table S2**), and the highest device performance occurred at 64 wt %, with an average PCE, J_{SC} and FF of 3.6 %, 8.5 mA cm⁻² and 0.42, respectively. PCEs are lower compared to O-IDTBR, which is likely largely due to the negligible LUMO-LUMO offset limiting J_{SC} and FF ,^[31] but ensuring a high V_{OC} varying between 1.02 V to 1.04 V across compositions. A similar trend as that for O-IDTBR is

observed, although weaker, whereby average PCE and J_{SC} peak around the estimated monotectic composition, despite the low acceptor crystallinity observed from DSC around this composition window. This suggests that the miscibility with the polymer donor is more important for morphology optimization compared to the acceptor degree of crystallinity in the blend.

3. Discussion

The observation of monotectic phase behavior in blends incorporating PffBT4T-2DT with either O-IDTBR or O-IDFBR raises the question of the impact of such behavior on the morphology as a function of D/A ratio in comparison to eutectic blends which have dominated the literature so far. Ideal BHJ morphology depends on a myriad of parameters, such as the presence of pure donor and acceptor domains and their size, as well as the composition of the mixed amorphous phase (if present). The relative importance of each parameter in optimizing device morphology depends on the properties of each component and their compatibility with one another. The suggested model for rationalizing optimal D/A ratios in eutectic blends is based on the need for pure acceptor percolation pathways,^[24] although the length scale of phase separation is also evidently crucial. Based on our case study of PffBT4T-2DT/NFA blends, our results suggest that controlling the degree of phase separation dictates the optimal morphology in these monotectic blends. We propose that the key parameter to control in such blends is the degree of L-L phase separation which is governed by the strength of S-L demixing (i.e., polymer aggregation), thus dictating the phase separation length scale and preventing large scale phase separation. Results also suggest that the miscibility of the acceptor with the polymer influences the balance between S-L and L-L demixing, such that using a more miscible acceptor (O-IDFBR in this case) requires a higher acceptor loading to optimize performance. In contrast, the degree of crystallinity of the NFA in the blend seems to have a less important effect on optimal D/A ratio.^[10] To further elucidate the similarities/differences compared to fullerene-based blends, we note that

PC71BM is known to display low levels of miscibility in blends with PffBT4T polymers.^[13] While the reported DSC thermograms for PffBT4T-2OD/PC71BM suggest eutectic behavior,^[29] visualizing the $T-\phi$ diagram evokes the case where the high melting temperature of the acceptor leads to a monotectic composition that is pushed towards the pure acceptor axis and a eutectic point which occurs at intermediate composition.^[36] This illustrates how in addition to the widely observed correlation between optimal D/A ratio and eutectic composition,^[8,16,24–27] additional insight into blend compatibility can be obtained from evaluating the shape of the liquidus curves constructed from DSC.

In our case study of PffBT4T-2DT:O-IDTBR, the suggested trend in morphology as a function of D/A ratio influences device performance by governing the trend in J_{SC} , FF , V_{OC} and voltage loss contributions seem to be largely insensitive to D/A ratio tuning, which is consistent with the observation of the same rate of charge decay at the different compositions due to a negligible change in the driving force for charge separation at the interface. This contrasts to what was recently observed for blends incorporating the amorphous polymer PBDTTT-EFT with EH-IDTBR, where charge dynamics were found to strongly depend on D/A ratio since increasing acceptor concentration above a threshold changed the morphology from an intimately mixed one-phase system to a two-phase system incorporating pure acceptor aggregates.^[44] In PffBT4T-2DT:O-IDTBR, the crystalline nature of the polymer leads to the formation of at least two phases across all the composition probed, making charge dynamics composition-independent.

The best performing device herein occurred at a D/A ratio around the monotectic composition. While GIWAXS and R-SoXS corroborate the occurrence of a coarser morphology at 74 wt % acceptor loading, exciton lifetime is largely insensitive towards composition. We suggest that the exciton dynamics from TAS are dominated by excitons which are generated in pure acceptor domains of similar size across all D/A ratios probed, while the increase in relative average purity and size scale concerns polymer/polymer-rich

domains. While higher purity is beneficial for charge extraction, the factor limiting J_{SC} at 74 wt % is likely poorer interconnectivity between pure crystalline polymer domains, leading to poorer hole extraction.

4. Conclusion

This study explores the effect of the interplay between polymer aggregation from solution (S-L demixing) and L-L demixing on morphology optimization by varying solution composition in blends of PffBT4T-2DT with two NFAs, O-IDTBR and O-IDFBR. The blend displays a complex hierarchical morphology with a monotonic increase of the median size scale as acceptor loading is increased. Finer phase separation at or below the monotectic composition ≈ 50 wt % O-IDTBR was assigned to the dominance of polymer aggregation (S-L demixing) during microstructure formation compared to more acceptor-rich compositions, where L-L demixing likely dominates. The low polymer concentration at 74 wt %, combined with excessive phase separation, is considered as the factor limiting J_{SC} by reducing the probability of efficient hole extraction via crystalline polymer domains. Another limiting factors of these blends is the negligible LUMO-LUMO offset which leads to the dominance of geminate recombination. By varying the degree of crystallinity of the acceptor, we find that it has a negligible influence on D/A ratio tuning as amorphous O-IDFBR displays a similar trend compared to crystalline O-IDTBR, although much weaker as device performance in the former system is limited by the even smaller LUMO-LUMO offset.^[31]

While previous studies investigate the morphology dependence on various parameters for PffBT4T polymers with fullerenes, this is to the best of our knowledge the first report which focuses on blends with NFAs. The robustness of PffBT4T polymer crystallization has been repeatedly observed and suggested to dominate microstructure formation in blends with fullerenes.^[21,30] Herein, the aggregation of PffBT4T-2DT is suggested to play a crucial role in controlling the degree of phase separation with two non-fullerene acceptors with very different crystallization behavior, highlighting the importance of donor/acceptor miscibility

over acceptor crystallinity on the interplay between S-L and L-L demixing. The experimental observation of monotectic phase behavior is interesting in that it contrasts with the dominance of eutectics in OPV literature so far and builds upon the rational understanding of D/A ratio optimization based on $T-\phi$ diagrams. Although limited in scope and far from quantitative, this study brings together the simplicity of bulk crystalline morphology evaluation from DSC with the importance of compatibility considerations, as highlighted by the growing number of quantitative investigation of component miscibility.

5. Experimental Section

Materials: PffBT4T-2DT, O-IDTBR and O-IDFBR were synthesised according to literature procedures,^[43,46-48] and reactions were carried out under an inert argon atmosphere using conventional Schlenk techniques. All other chemicals and solvents were purchased from Sigma Aldrich¹ and Acros Organics and used as received.

OPV Device Fabrication and Characterization: Inverted architecture bulk heterojunction solar cells (glass/ITO/ZnO/PffBT4T-2DT:NFA/MoO₃/Ag) were fabricated as follows. Glass substrates, prepatterned with ITO (15 Ω sheet resistance per square), were cleaned by sonication in acetone, detergent, deionized water, and isopropanol before oxygen plasma treatment for 10 min. A layer of ZnO, \approx 30 nm (from Zn(OAc)₂ in monoethanolamine (60 μ L) and 2-methoxyethanol (2 mL)), was deposited by spin-coating onto the ITO substrate at 4000 r.p.m. for 40 s, followed by annealing at 150 $^{\circ}$ C for 20 min. Active layer solutions (PffBT4T-2DT:NFA, of varying weight ratios) were prepared from CB with a total concentration of 15 mg mL⁻¹, unless otherwise stated. The solutions were heated to 80 $^{\circ}$ C overnight, and the active layers were deposited by spin-coating from hot solution and substrates (100 $^{\circ}$ C) at 2500

¹ Certain commercial equipment, instruments, materials or software are identified in this paper in order to specify the experimental procedure adequately. Such identification is not intended to imply recommendation or endorsement by the National Institute of Standards and Technology, nor is it intended to imply that the materials or equipment identified are necessarily the best available for the purpose.

r.p.m. (262 rad/s) for 1 min. The active layers were then annealed at 80 °C for 5 min, under an inert atmosphere. A MoO₃ anode interlayer (10 nm) and Ag anode (100 nm) were then deposited by thermal evaporation through a shadow mask, giving an active area of 0.045 cm² per device. The *J-V* characteristics were measured under AM1.5G (100 mW cm⁻²) irradiation using an Oriel Instruments Xenon lamp calibrated to a Si reference cell to correct for spectral mismatch, and a Keithley 2400 source meter. Device active layer thicknesses were determined using a Veeco Dektak 150 profilometer.

Differential Scanning Calorimetry: Samples for DSC were prepared by drop-casting neats and blends from chlorobenzene solutions. Two heating and two cooling cycles were recorded at a rate of 5 °C min⁻¹. A Mettler Toledo DSC 1 was used for neats and blends of the 41 kDa PffBT4T-2DT batch and a TA Instruments DSC Q20 was used for the neat and blends of the 55 kDa polymer.

Low-Angle Annular Dark-Field Scanning Transmission Electron Microscopy (LAADF-STEM): Blend solutions of 41 kDa PffBT4T-2DT with either NFA of varying weight ratios were prepared from CB with a total concentration of 15 mg mL⁻¹ unless stated otherwise. The solutions were heated to 80 °C overnight, and the active layers were deposited on Si (University Wafer) substrates coated with a water soluble sacrificial layer (PEDOT:PSS) (Sigma Aldrich) by spin-coating from hot solution and substrates (100 °C) at 2500 r.p.m. for 1 min. The samples were then annealed at 80 °C for 5 min, under nitrogen atmosphere. The films were then scored with a scalpel, and immersed in de-ionized water to dissolve the sacrificial layer. The delaminated BHJ films floating on the water surface were collected with a copper mesh TEM grid with a lacey carbon coating and allowed to dry in air prior to analysis. LAADF-STEM images were acquired with a FEI Titan 80-300 at operating voltage of 300 kV. A 10 micron probe-forming aperture was employed to maximize the depth of focus resulting in a probe convergence angle of 3 mrad and a probe current of 60

pA. An annular dark field detector was employed to collect the scattered dark-field image signal over an angular range of 17 mrad to 96 mrad.

Grazing Incidence X-ray Wide Angle Scattering: GIWAXS measurements were performed at the 11-BM Complex Materials Scattering (CMS) beamline of the National Synchrotron Light Source II (NSLS-II) with a beam energy of 10 keV. The 2D scattering patterns were collected at an X-ray incidence angle of 0.14° with a Pilatus 300K detector with a pixel size of 172 μm and placed about 150 mm from the sample. The data were analyzed using Nika analysis package based on Igor Pro.^[49] Sector averaged 1D scattering profiles were obtained from 15° cake sectors. Volume normalized pole figures were constructed from the 2D GIWAXS images corrected for the missing wedge by integrating the intensities at each detector azimuth within the q range of the lamellar diffraction peak. A linear background defined by the intensities at the two ends of the integrated q range was subtracted. The relative degree of crystallinity (rDoC) was calculated by integrating the intensities over the crystallographic orientation sphere: $\text{rDoC} = \int_0^{\pi/2} I(\chi) \sin \chi d\chi$. Film thicknesses were measured using an ellipsometer (M-2000-XI, J. A. Woollam Co., Inc) and were found to be in the range 210 nm to 290 nm.

Resonant-Soft X-ray Scattering: The scattering contrast is directly proportional to $\Delta n^2 = \Delta\delta^2 + \Delta\beta^2$, where $1 - \delta$ is the real part (related to dispersion) and β is the imaginary part (related to absorption) of the complex refractive index. R-SoXS measurements were performed in transmission geometry at the ALS beamline 11.0.1.2^[50] following procedures described earlier.^[51] BHJ films were cast directly onto UV-Ozone treated 100 nm Si_3N_4 windows (Norcada).^[50] The 2-D R-SoXS data were collected at beamline 11.0.1.2 at the Advanced Light Source using a Peltier cooled (-45°C) in-vacuum (base pressure $\approx 10^{-9}$ kPa (10^{-8} mBar)) CCD detector (PI-MTE, Princeton Instruments, 2048×2048 pixels). 1-D scattering profiles were obtained from the reduction of the 2-D scattering patterns using a custom Nika^[49]

analysis package and subsequently normalized for the instantaneous X-ray flux. The scattering intensity is affected by the distance travelled by the X-ray beam through the sample as well as the scattering volume. R-SoXS scattering intensities were therefore normalized for absorption and film thickness.^[52] Film thicknesses were measured using an ellipsometer (M-2000-XI, J. A. Woollam Co., Inc). Films processed from 15 mg mL⁻¹ solutions had thicknesses ranging between 230 nm to 290 nm. R-SoXS contrast calculations were done using PEY near edge X-ray absorption fine structure (NEXAFS) spectroscopy on films cast on Si substrate at the Spectroscopy Soft and Tender (SST-1) beamline at NSLS-II. The QANT^[53] package based on Igor Pro was used to analyze the NEXAFS data.

Photoluminescence spectroscopy: PL spectra were acquired using a home-built set up with an Andor SR-163 spectrometer and a CCD array (Andor i-DUS). The excitation source provided the excitation wavelength of 630 nm (1.96 eV photon energy) and a low pass filter (650 nm) was in place to attenuate incident beam reflection. The emitted light was collected perpendicular to excitation focused into an optical fiber. The spectra were measured at 100 accumulated exposures of 0.1 s. Corrections were made by subtracting the constant background and accounting for the detector response, no change were made to the optical configuration between measurements. PL spectra were normalized with respect to the absorbance at the excitation wavelength.

TAS: A broadband pump-probe fs TA spectrometer Helios (Spectra Physics, Newport Corp.) was used to measure the TA spectra and kinetics for thin film samples. Ultrafast laser pulses (800 nm, 100 fs pulse duration) were generated by a 1 kHz Ti:sapphire regenerative amplifier (Solstice, Spectra Physics). One portion of the 800 nm pulses was directed to an optical parametric amplifier (TOPAS) to generate the visible pump pulses at 650 nm. The rest of the 800 nm pulses routes onto a mechanical delay stage (6 ns time window) and is directed through a sapphire crystal to generate white light probe ranging from (800 to 1600) nm in the near-infrared region. The pump and probe beams were focused onto the same spot on the

samples. During the measurements, all the samples were kept in a quartz cuvette under continuous N₂ flow. Samples were excited at a pump fluence of 5 μJ cm⁻² unless otherwise stated.

External Quantum Efficiency Measurements: EQE measurements were carried out using a grating spectrometer (CS260-RG-4-MT-D) to create monochromatic light from a tungsten halogen light source. The light was chopped at 300Hz, and a Stanford Research System SR830 lock-in amplifier was used to detect the photocurrent. Long pass filters at (610, 780, 850 and 1000) nm were used to filter out scattered light from the monochromator. The spectra were calibrated using a Silicon photodiode.

Electroluminescence Measurements: EL and PL spectra were recorded using a Shamrock 303 spectrograph combined with a iDUS InGaAs array detector which was cooled to -90 °C. The obtained EL intensity spectra were calibrated with the spectrum from a calibrated Halogen lamp.

Supporting Information

Supporting Information is available from the Wiley Online Library or from the author.

Acknowledgements

ZH thanks the EPSRC for a doctoral studentship. The authors thank KAUST for financial support, and acknowledge EPSRC Projects EP/G037515/1, EP/M005143/1 and EP/L016702/1, and EC FP7 Project SC2 (610115), ECH2020 (643791). JN acknowledges funding from the EPSRC (grant number EP/P005543/1) and the European Research Council (Project CAPaCITY, Grant agreement No. 742708). ES thanks the Fonds de Recherche du Quebec-Nature et technologies (FRQNT) for a post-doctoral fellowship. AAYG thanks the EPSRC for award of a post-doctoral fellowship (grant number EP/P00928X/1). MA thanks the EPSRC for a doctoral studentship. Portions of this research were carried out at the 7-ID Spectroscopy Soft and Tender (SST-1), 11-BM Complex Materials Scattering (CMS) beamlines of the National Synchrotron Light Source II, a U.S. Department of Energy (DOE) Office of Science User Facility operated for the DOE Office of Science by Brookhaven National Laboratory under Contract No. DE-SC0012704, and at beamline 11.0.1.2 of the Advanced Light Source, which is supported by the Director, Office of Science, Office of Basic Energy Sciences, of the U.S. Department of Energy under contract no. DE-AC02-05CH11231. D. Fischer, C. Jaye, E. Gann, R. Li (NSLS-II) and C. Wang (ALS) are acknowledged for assisting with the experiments.

Received: ((will be filled in by the editorial staff))

Revised: ((will be filled in by the editorial staff))

Published online: ((will be filled in by the editorial staff))

References

- [1] W. Zhao, S. Li, H. Yao, S. Zhang, Y. Zhang, B. Yang, J. Hou, *J. Am. Chem. Soc.* **2017**, *139*, 7148.
- [2] J.-D. Chen, Y.-Q. Li, J. Zhu, Q. Zhang, R.-P. Xu, C. Li, Y.-X. Zhang, J.-S. Huang, X. Zhan, W. You, J.-X. Tang, *Adv. Mater.* **2018**, *30*, 1706083.
- [3] X. Xu, T. Yu, Z. Bi, W. Ma, Y. Li, Q. Peng, *Adv. Mater.* **2018**, *30*, 1703973.
- [4] S. Li, L. Ye, W. Zhao, H. Yan, B. Yang, D. Liu, W. Li, H. Ade, J. Hou, *J. Am. Chem. Soc.* **2018**, *140*, 7159.
- [5] J. Yuan, Y. Zhang, L. Zhou, G. Zhang, H.-L. Yip, T.-K. Lau, X. Lu, C. Zhu, H. Peng, P. A. Johnson, M. Leclerc, Y. Cao, J. Ulanski, Y. Li, Y. Zou, *Joule* **2019**, *3*, 1140.
- [6] X. Che, Y. Li, Y. Qu, S. R. Forrest, *Nat. Energy* **2018**, *3*, 422.
- [7] C. B. Nielsen, S. Holliday, H.-Y. Chen, S. J. Cryer, I. McCulloch, *Acc. Chem. Res.* **2015**, *48*, 2803.
- [8] A. Wadsworth, Z. Hamid, M. Bidwell, R. S. Ashraf, J. I. Khan, D. H. Anjum, C. Cendra, J. Yan, E. Rezasoltani, A. A. Y. Guilbert, M. Azzouzi, N. Gasparini, J. H. Bannock, D. Baran, H. Wu, J. C. de Mello, C. J. Brabec, A. Salleo, J. Nelson, F. Laquai, I. McCulloch, *Adv. Energy Mater.* **2018**, *8*, 1801001.
- [9] N. Li, I. McCulloch, C. J. Brabec, *Energy Environ. Sci.* **2018**, *11*, 1355.
- [10] C. Zhang, S. Langner, A. V Mumyatov, D. V Anokhin, J. Min, J. E. Da Io Perea, K. L. Gerasimov, A. Osvet, D. A. Ivanov, P. Troshin, N. Li, C. J. Brabec, *J. Mater. Chem. A* **2017**, *5*, 17570.
- [11] J. Perea, S. Langner, M. Salvador, B. Sanchez-Lengeling, N. Li, C. Zhang, G. Jarvas, J. Kontos, A. Dallos, A. Aspuru-Guzik, C. J. Brabec, *J. Phys. Chem. C* **2017**, *121*, 18153.
- [12] L. Ye, H. Hu, M. Ghasemi, T. Wang, B. A. Collins, J.-H. Kim, K. Jiang, J. H. Carpenter, H. Li, Z. Li, T. McAfee, J. Zhao, X. Chen, J. Lin Yuk Lai, T. Ma, J.-L.

- Bredas, H. Yan, H. Ade, *Nat. Mater.* **2018**, *17*, 253.
- [13] L. Ye, B. A. Collins, X. Jiao, J. Zhao, H. Yan, H. Ade, *Adv. Energy Mater.* **2018**, *8*, 1703058.
- [14] L. Krückemeier, P. Kaienburg, J. Flohre, K. Bittkau, I. Zonno, B. Krogmeier, T. Kirchartz, *Commun. Phys.* **2018**, *1*, 27.
- [15] T. M. Burke, M. D. McGehee, *Adv. Mater.* **2014**, *26*, 1923.
- [16] F. C. Jamieson, E. B. Domingo, T. McCarthy-Ward, M. Heeney, N. Stingelin, J. R. Durrant, *Chem. Sci.* **2012**, *3*, 485.
- [17] P. Rathi, T.-M. Huang, P. Dayal, T. Kyu, *J. Phys. Chem. B* **2008**, *112*, 6460.
- [18] S. Nilsson, A. Bernasik, A. Budkowski, E. Moons, *Macromolecules* **2007**, *40*, 8291.
- [19] C. McDowell, M. Abdelsamie, M. F. Toney, G. C. Bazan, *Adv. Mater.* **2018**, *30*, 1707114.
- [20] L. Yu, D. Qian, S. Marina, F. A. A Nugroho, A. Sharma, S. Hultmark, A. I. Hofmann, R. Kroon, J. Benduhn, D.-M. Smilgies, K. Vandewal, M. R. Andersson, C. Langhammer, J. Martín, F. Gao, C. Mu, *ACS Appl. Mater. Interfaces* **2019**, *11*, 21766.
- [21] Y. Liu, J. Zhao, Z. Li, C. Mu, W. Ma, H. Hu, K. Jiang, H. Lin, H. Ade, H. Yan, *Nat. Commun.* **2014**, *5*, 5293.
- [22] Y. Kim, S. Cook, S. M. Tuladhar, S. A. Choulis, J. Nelson, J. R. Durrant, D. D. C. Bradley, M. Giles, I. McCulloch, C.-S. Ha, M. Ree, *Nat. Mater.* **2006**, *5*, 197.
- [23] H. Hu, P. C. Y. Chow, G. Zhang, T. Ma, J. Liu, G. Yang, H. Yan, *Acc. Chem. Res.* **2017**, *50*, 2519.
- [24] C. Müller, T. A. M. Ferenczi, M. Campoy-Quiles, J. M. Frost, D. D. C. Bradley, P. Smith, N. Stingelin-Stutzmann, J. Nelson, *Adv. Mater.* **2008**, *20*, 3510.
- [25] P. Wolfer, P. E. Schwenn, A. K. Pandey, Y. Fang, N. Stingelin, P. L. Burn, P. Meredith, *J. Mater. Chem. A* **2013**, *1*, 5989.
- [26] N. C. Miller, R. Gysel, C. E. Miller, E. Verploegen, Z. Beiley, M. Heeney, I.

- McCulloch, Z. Bao, M. F. Toney, M. D. McGehee, *J. Polym. Sci. Part B: Polym. Phys.* **2011**, *49*, 499.
- [27] C. Muller, J. Bergqvist, K. Vandewal, K. Tvingstedt, A. S. Anselmo, R. Magnusson, M. I. Alonso, E. Moons, H. Arwin, M. Campoy-Quiles, O. Inganäs, *J. Mater. Chem.* **2011**, *21*, 10676.
- [28] J. Zhao, Y. Li, G. Yang, K. Jiang, H. Lin, H. Ade, W. Ma, H. Yan, *Nat. Energy* **2016**, *1*, 15027.
- [29] N. Li, J. D. Perea, T. Kassar, M. Richter, T. Heumueller, G. J. Matt, Y. Hou, N. S. Güldal, H. Chen, S. Chen, S. Langner, M. Berlinghof, T. Unruh, C. J. Brabec, *Nat. Commun.* **2017**, *8*, 14541.
- [30] W. Ma, G. Yang, K. Jiang, J. H. Carpenter, Y. Wu, X. Meng, T. McAfee, J. Zhao, C. Zhu, C. Wang, H. Ade, H. Yan, *Adv. Energy Mater.* **2015**, *5*, 1501400.
- [31] D. Baran, T. Kirchartz, B. S. Wheeler, S. Dimitrov, M. Abdelsamie, J. Gorman, R. S. Ashraf, S. Holliday, A. Wadsworth, N. Gasparini, P. Kaienburg, H. Yan, A. Amassian, C. J. Brabec, J. R. Durrant, I. McCulloch, *Energy Environ. Sci.* **2016**, *9*, 3783.
- [32] H. Cha, S. Wheeler, S. Holliday, S. D. Dimitrov, A. Wadsworth, H. H. Lee, D. Baran, I. McCulloch, J. R. Durrant, *Adv. Funct. Mater.* **2018**, *28*, 1704389.
- [33] H. Cha, J. Wu, A. Wadsworth, J. Nagitta, S. Limbu, S. Pont, Z. Li, J. Searle, M. F. Wyatt, D. Baran, J.-S. Kim, I. McCulloch, J. R. Durrant, *Adv. Mater.* **2017**, *29*, 1701156.
- [34] A. Wadsworth, R. S. Ashraf, M. Abdelsamie, S. Pont, M. Little, M. Moser, Z. Hamid, M. Neophytou, W. Zhang, A. Amassian, J. R. Durrant, D. Baran, I. McCulloch, *ACS Energy Lett.* **2017**, *2*, 1494.
- [35] A. A. Y. Guilbert, L. X. Reynolds, A. Bruno, A. Maclachlan, S. P. King, M. A. Faist, E. Pires, J. E. Macdonald, N. Stingelin, S. A. Haque, J. Nelson, *ACS Nano* **2012**, *6*, 3868.

- [36] W. R. Burghardt, *Macromolecules* **1989**, *22*, 2482.
- [37] R. A. Matkar, T. Kyu, *J. Phys. Chem. B* **2006**, *110*, 12728.
- [38] T. Zhang, E. Birgersson, J. Luther, *Appl. Phys. Express* **2015**, *8*, 24301.
- [39] F. Piersimoni, S. Chambon, K. Vandewal, R. Mens, T. Boonen, A. Gadisa, M. Izquierdo, S. Filippone, B. Ruttens, J. D. ' Haen, N. Martin, L. Lutsen, D. Vanderzande, P. Adriaensens, J. V Manca, *J. Phys. Chem. C* **2011**, *115*, 10873.
- [40] H. W. Ro, J. M. Downing, S. Engmann, A. A. Herzing, D. M. Delongchamp, L. J. Richter, S. Mukherjee, H. Ade, M. Abdelsamie, L. K. Jagadamma, A. Amassian, Y. Liu, H. Yan, *Energy Environ. Sci.* **2016**, *9*, 2835.
- [41] B. A. Collins, Z. Li, J. R. Tumbleston, E. Gann, C. R. McNeill, H. Ade, *Adv. Energy Mater.* **2013**, *3*, 65.
- [42] W. Zhang, R. Hu, X. Zeng, X. Su, Z. Chen, X. Zou, J. Peng, C. Zhang and A. Yartsev, *Polymers* **2019**, *11*, 408.
- [43] S. Holliday, R. S. Ashraf, A. Wadsworth, D. Baran, S. A. Yousaf, C. B. Nielsen, C.-H. Tan, S. D. Dimitrov, Z. Shang, N. Gasparini, M. Alamoudi, F. Laquai, C. J. Brabec, A. Salleo, J. R. Durrant, I. McCulloch, *Nat. Commun.* **2016**, *7*, 11585.
- [44] H. Cha, G. Fish, J. Luke, A. Alraddadi, H. H. Lee, W. Zhang, Y. Dong, S. Limbu, A. Wadsworth, I. P. Maria, L. Francàs, H. L. Sou, T. Du, J. Kim, M. A. McLachlan, I. McCulloch, J. R. Durrant, *Adv. Energy Mater.* **2019**, *9*, 1901254.
- [45] Y. Dong, H. Cha, J. Zhang, S. Tuladhar, I. McCulloch, J. R. Durrant, A. A. Bakulin, *J. Chem. Phys.* **2019**, *150*, 104704.
- [46] D. Baran, R. S. Ashraf, D. A. Hanifi, M. Abdelsamie, N. Gasparini, J. A. Röhr, S. Holliday, A. Wadsworth, S. Lockett, M. Neophytou, C. J. M. Emmott, J. Nelson, C. J. Brabec, A. Amassian, A. Salleo, T. Kirchartz, J. R. Durrant, I. McCulloch, *Nat. Mater.* **2017**, *16*, 363.
- [47] Z. Chen, P. Cai, J. Chen, X. Liu, L. Zhang, L. Lan, J. Peng, Y. Ma, Y. Cao, *Adv.*

- Mater.* **2014**, *26*, 2586.
- [48] S. Holliday, R. S. Ashraf, C. B. Nielsen, M. Kirkus, J. A. Röhr, C.-H. Tan, E. Collado-Fregoso, A.-C. Knall, J. R. Durrant, J. Nelson, I. McCulloch, *J. Am. Chem. Soc.* **2015**, *137*, 898.
- [49] J. Ilavsky, *J. Appl. Crystallogr.* **2012**, *45*, 324.
- [50] E. Gann, A. T. Young, B. A. Collins, H. Yan, J. Nasiatka, H. A. Padmore, H. Ade, A. Hexemer, C. Wang, *Rev. Sci. Instrum.* **2012**, *83*, 045110.
- [51] B. A. Collins, J. E. Cochran, H. Yan, E. Gann, C. Hub, R. Fink, C. Wang, T. Schuettfort, C. R. McNeill, M. L. Chabiny, H. Ade, *Nat. Mater.* **2012**, *11*, 536.
- [52] J. R. Tumbleston, A. C. Stuart, E. Gann, W. You, H. Ade, *Adv. Funct. Mater.* **2013**, *23*, 3463.
- [53] E. Gann, C. R. McNeill, A. Tadich, B. C. C. Cowie, L. Thomsen, *J. Synchrotron Radiat.* **2016**, *23*, 374.

The dependence of performance on composition in organic solar cells based on PffBT4T-2DT polymer with O-IDTBR or O-IDFBR as non-fullerene acceptor is investigated. The effect on morphology is discussed in terms of the interplay between immiscibility, inferred from phase behavior, and polymer aggregation. Morphology is optimized when polymer crystallite interconnectivity and size are balanced.

Keyword: Organic Photovoltaics

Z. Hamid, A. Wadsworth, E. Rezasoltani, S. Holliday, M. Azzouzi, M. Neophytou, A. A. Y. Guilbert, Y. Dong, M. S. Little, S. Mukherjee, A. A. Herzing, H. Bristow, R. J. Kline, D. M. DeLongchamp, A. A. Bakulin, J. Durrant, J. Nelson and I. McCulloch*

Influence of Polymer Aggregation and Liquid Immiscibility on Morphology Tuning by Varying Composition in PffBT4T-2DT/Non-Fullerene Organic Solar Cells

